Genesis of corrugated fault surfaces by strain localization recorded at oceanic detachments

- 4 Ross Parnell-Turner¹, Javier Escartín², Jean-Arthur Olive³, Deborah K. Smith⁴, and
- 5 Sven Petersen⁵
- 6 ¹Department of Geology and Geophysics, Woods Hole Oceanographic Institution, Woods
- 7 Hole, Massachusetts 02543, USA
- 8 ²CNRS / Institut de Physique du Globe de Paris, 1 rue Jussieu, 75005, Paris, France.
- 9 ³Laboratoire de Géologie, Ecole Normale Supérieure / CNRS UMR 8538, PSL Research
- 10 University, 24 rue Lhomond, 75005, Paris, France.
- ⁴National Science Foundation, 2415 Eisenhower Ave., Alexandria, VA, 22314, USA.
- 12 ⁵GEOMAR / Helmholtz Centre for Ocean Research, Wischhofstrasse 1-3, 24148, Kiel,
- *Germany*.

Keywords

Oceanic detachment faulting; mid-ocean ridge; corrugations

Abstract

Seafloor spreading at slow and ultraslow rates is often taken up by extension on large-offset faults called detachments, which exhume lower crustal and mantle rocks, and in some cases make up domed oceanic core complexes. The exposed footwall may reveal a characteristic pattern of spreading-parallel corrugations, the largest of which are clearly visible in multibeam bathymetric data, and whose nature and origin have been the subject of controversy. In order to tackle this debate, we use available near-bottom bathymetric surveys recently acquired with autonomous deep-sea vehicles over five corrugated detachments along the Mid-Atlantic Ridge. With a spatial resolution of 2 m, these data allow us to compare the geometry of corrugations on oceanic detachments that are characterized by differing fault zone lithologies, and accommodate varying amounts of slip. The fault surfaces host corrugations with wavelengths of 10–250 m, while individual corrugations are finite in length, typically 100–500 m. Power spectra of profiles calculated across the corrugated fault surfaces reveal a common level of roughness, and

indicate that the fault surfaces are not fractal. Since systematic variation in roughness with fault offset is not evident, we propose that portions of the exposed footwalls analyzed here record constant brittle strain. We assess three competing hypotheses for corrugation formation and find that the continuous casting and varying depth to brittle-ductile transition models cannot explain the observed corrugation geometry nor available geological observations. We suggest a model involving brittle strain localization on a network of linked fractures within a zone of finite thickness, which we term the corrugation factory, is a better explanation for the observations. This model explains corrugations on oceanic detachment faults exposed at the seafloor and on normal faults in the continents, and is consistent with recently imaged corrugations on a subduction zone megathrust. Hence fracture linkage and coalescence may give rise to corrugated fault zones, regardless of earlier deformation history and tectonic setting.

1. Introduction

Large-offset normal faults, known as detachments, are now understood to play a significant role in accommodating plate separation at slow- and ultraslow-spreading midocean ridges (e.g. Escartín and Canales, 2011). This style of crustal accretion accounts for seafloor formation in large parts of the Atlantic, Indian and Arctic Oceans; for example, up to 50% of lithosphere accreted along the Mid-Atlantic Ridge (MAR) between 12.5° and 35°N is thought to be formed in the presence of detachment faults (Escartín et al., 2008). Seafloor spreading under these conditions leads to the exhumation of lower crustal and mantle rocks on the seafloor forming domes that can be tens of kilometers in width called oceanic core complexes (OCCs; e.g. Karson and Dick, 1983). These domes are exposed detachment fault footwalls, which preserve a history of ductile and brittle deformation, in a setting where magmatism and slip play important roles (e.g. Karson et al., 2006; Schroeder and John, 2004). The upper surface of OCCS are often characterized by spreading-parallel corrugations, which have been compared to those found on terrestrial normal faults (e.g. Whitney et al., 2013), and more recently, to those imaged on a subduction zone megathrust (Edwards et al., 2018).

Early seafloor mapping efforts revealed oceanic detachment corrugations with wavelengths of a few kilometers to hundreds of meters (Figure 1a; e.g. Tucholke et al.,

1998), however observations were limited by the ~100 m spatial resolution of shipmounted multibeam systems at the time. Images acquired using deep-towed sonars also revealed lineations at smaller spatial scales, superimposed on these larger-scale bathymetric corrugations (Cann et al., 1997; MacLeod et al., 2009; Searle et al., 2003). Recent developments in near-bottom mapping using autonomous underwater vehicles (AUVs) at ~1–2 m resolution have revealed much smaller wavelength (~10 m) oscillations in fault topography, superimposed upon previously known bathymetric corrugations (Figure 1b). Recent submersible dives have revealed meter-scale corrugations and striations at outcrop scale (Figure 1c; Escartín et al., 2017; Bonnemains et al., 2017), and spreading-parallel striations on the cm-scale in hand specimen (Figure 1d; Bonnemains et al., 2017). Hence while it is now well-established that corrugations occur on a wide range of scales, the mechanisms of corrugation development remain controversial, due to a lack of comparable quantitative observations across multiple sites.

The largest, kilometer-scale undulations have been compared to networks of cuspate fault scarps (John, 1987), and to shortening features seen on the footwalls of terrestrial detachments undergoing compression (Fletcher and Bartley, 1994; Tucholke et al., 1998). Karson (1999) suggested that undulations on the Kane massif on the MAR are ridge-perpendicular faulted blocks accommodating extension, although more recent observations at higher resolution have shown this to be unlikely (e.g. MacLeod et al., 2002). It has also been suggested that corrugations on the scale of hundreds of meters could arise due to depth variations in the brittle-ductile transition on which the fault roots (Tucholke et al., 2008). Alternatively, corrugations could arise due to the molding of a plastic or partially molten footwall in contact with a strong, brittle hanging wall, in a process termed continuous casting (Spencer, 1999). More recently, corrugations on detachment fault exposures at 13°N on the Mid-Atlantic Ridge have been explored by a combination of AUV surveys, remotely operated vehicle (ROV) observations and sampling (Escartín et al., 2017). These near-bottom observations have led to a suggestion that strain localization within an anastomosing three-dimensional network of fault segments results in corrugation formation (Escartín et al., 2017).

In order to evaluate these competing hypotheses for the origin of corrugations, we use near-bottom bathymetric data acquired in recent years by AUVs at five OCCs on the MAR to quantify the fine-scale structure and morphology of exposed fault planes. Our objective is to characterize the geometry of meter- to kilometer-scale corrugations, and

compare these across detachments of differing age and lithology in order to test hypotheses regarding their origins. We then use these observations of corrugation geometry to constrain simple thermal and mechanical arguments for corrugation formation that are implied by the different hypotheses. Finally, we use spectral analyses of the fault surfaces to examine variations in fault roughness between the five study locations. Fault roughness plays a key role in fault and earthquake mechanics, and here we explore the possible implications for corrugation formation.

2. Study Sites and Data Acquisition

We use near-bottom multibeam bathymetric data acquired using AUVs at five locations on the MAR to study fine-scale corrugations (Figures 2 and 3): one at the Trans-Atlantic Geotraverse (TAG) segment; two at the 16.5°N segment (16°36'N and South Core Complex; SCC) and two at the 13°N segment (13°20'N and 13°30'N). Well-developed OCCs, with varying lengths of exposed fault surface (a proxy for displacement on the fault surface), are found at these locations, providing an opportunity to compare the morphology of fine-scale corrugations at high resolution (~1m).

2.1 TAG Detachment Fault

- A 30 km-wide, domed OCC is located on the eastern flank of the MAR at the TAG segment near 26.17°N, with full spreading rate of 21 km Ma⁻¹ (Figure 2b; Tivey et al., 2003). This well-studied segment hosts numerous inactive hydrothermal mounds and a large active hydrothermal vent field on the detachment hanging wall (e.g. Rona et al., 1993). Age dating suggests that intermittant hydrothermal activity within this segment started as early as 140 ka ago (Lalou et al., 1995), while intense microearthquake activity indicates that the fault is active today (deMartin et al., 2007). Human-occupied submersible dives by ALVIN and MIR found significant mass wasting on the upper slopes of the footwall (chaotic terrain, defined below), however in-situ observations and sampling of the exposed corrugated footwall mapped during the AUV survey presented here are lacking, meaning that the footwall lithology remains uncertain (Karson and Rona, 1990; Zonenshain et al., 1989).
- Near-bottom bathymetric data were acquired over a small, corrugated portion of the TAG detachment during AUV *Abyss* dive 235 as part of RV *Meteor* Cruise M127 in

June 2016 (GEOMAR, Germany). The corrugations were undetected by shipboard multibeam sonars until being mapped by AUV. *Abyss* surveyed at 80 m above the seafloor at an average velocity of ~3 kt (1.54 m s⁻¹), carrying a RESON 7125 multibeam sonar operating at 200 kHz. Navigation was achieved using two long baseline transponders deployed on the seabed, and the data were processed using MB-System software to produce a ~2 m horizontal resolution grid (Figure 3a).

2.2 South Core Complex and OCC 16°36'N

The 16.5°N segment of the MAR, located ~100 km north of the Fifteen-Twenty Fracture Zone, is characterized by numerous detachment faults and OCC domes distributed on both sides of the axis, which is spreading at a rate of ~21 km Ma⁻¹ (Parnell-Turner et al., 2016; Smith et al., 2014). Here, we use near-bottom bathymetric data acquired over two corrugated surfaces in the 16.5°N area. The first is a ~10 km-wide domed, corrugated detachment fault called South Core Complex (SCC) located west of the axis, clearly identified from shipboard bathymetric data (Figure 3c). Rock samples dredged from this fault surface included gabbro and serpentinized peridotite (Smith et al., 2014). Second, we examine a ~5 km-wide corrugated surface located 20 km north of SCC at 16°36'N (Figure 3b), where dredges containing diabase, diabase breccia and peridotite were recovered (Smith et al., 2014). In common with TAG, these corrugations were not detected by shipboard multibeam sonars, while thin sediment cover shows that the fault at 16°36'N is likely to be slipping today (Parnell-Turner et al., 2014).

Near-bottom bathymetric surveys over SCC (dives 176, 177, and 180) and OCC 16°36'N (dive 181) were carried out using AUV *Sentry* (Woods Hole Oceanographic Institution, USA) in May 2013 during RV *Knorr* Cruise KN210-05 (Smith et al., 2014). *Sentry* flew at ~65 m above the seafloor at a velocity of ~1.5 kt (0.77 m s⁻¹) carrying a RESON 7125 multibeam sonar operating at 400 kHz. Navigation was achieved using an ultra-short baseline system, and the data were processed using MB-System software to produce a ~2 m horizontal resolution grid.

2.3 13°30'N and 13°20'N OCCs

A series of well-developed detachment faults and associated OCCs were first identified between 12°55' and 13°45'N along the MAR using shipboard bathymetry surveys and

seismicity detected by autonomous hydrophones (Smith et al., 2008). Near-bottom imaging revealed a 6 km-wide corrugated dome at 13°20'N, which is thought to represent ~0.4 Ma of slip (Figure 3e; MacLeod et al., 2009; Mallows and Searle, 2012). High rates of microearthquake activity are evident today (Parnell-Turner et al., 2017), while AUVbased water column studies and remotely-operated vehicle (ROV) dives revealed the presence of active high-temperature (~365°C) venting, the Irinovskoe vent field, near the crest of the dome (Escartín et al., 2017). A second OCC, 20 km to the north at 13°30'N, has similar corrugated morphology, however it is degraded by normal faulting, fissuring, mass-wasting, and hydrothermal deposition (see Escartín et al., 2017). These processes partially disrupt and modify the corrugations (Figure 3d). In-situ sampling using a remotely-operated vehicle (ROV) revealed contrasting lithologies at these two detachment zones: the 13°20'N corrugated surface is primarily basalt breccia, while gabbro and peridotite are more common at 13°30'N OCC (Escartín et al., 2017). Both the 13°20'N and 13°30'N OCCs host several inactive and active hydrothermal vent fields (Cherkashov et al., 2010). Near-bottom bathymetric data (doi:10.17882/48335) were acquired during 9 dives of AUV Abyss as part of the ODEMAR Cruise (doi:10.17600/13030070) onboard N/O Pourquoi Pas? in December 2013 (Escartín et al., 2017). Abyss flew at ~70 m above the seafloor carrying a RESON 7125 multibeam sonar operating at 200 kHz; resulting data were processed using MB-System and gridded at ~2 m horizontal spacing.

184185

164

165

166

167

168

169

170

171

172

173

174

175

176

177

178

179

180

181

182

183

3. Corrugation analysis

187

188

189

190

191

192

193

194

195

196

186

The near-bottom AUV bathymetric data described above reveal the detailed morphology of corrugations which is unresolved by shipboard multibeam data (Figure 1). Four distinct morphological terrains (defined in terms of bathymetric relief) can be defined at these OCCs, the complete sequence of which can be identified at the 13°20'N OCC (Figure 5e; for details see Escartín et al., 2017). First, nearest to the axis and occupying the rift valley floor is the volcanic terrain, which consists of hummocky seafloor, basalt flows and cones. Second, between the volcanic terrain and the hanging-wall cutoff (sometimes called the termination), is the apron, which is a narrow band (a few hundreds of meters to ~1 km wide) of relatively smooth seafloor that skirts the curved hanging-

wall cutoff and that the detachment drags and uplifts with respect to adjacent volcanic terrain. The hanging-wall cutoff itself often consists of a well-defined depression (described as a moat) that can be traced over a few km. This moat is tens to ~250 m wide, ~10–15 m deep and is interpreted to mark the transition from hanging wall to footwall (yellow arrows in Figure 4; Escartín et al, 2017). An apron bordering the hanging-wall cutoff is also observed at the TAG and 16°N segment OCCs. Third is the fault surface itself, that emerges adjacent to the hanging-wall cutoff, and is characterized by spreading-parallel corrugations. Irregularly distributed rubble ridges are sometimes observed in depressions between the km-scale corrugations (16°36'N and 13°20'N OCCs; Figures 4 and 5). These ridges, typically ~100–150 m long, 2–4 m in relief and oriented parallel to the hanging-wall cutoff, may represent apron material which has episodically slumped onto the detachment footwall (Escartín et al., 2017). Fourth, the chaotic terrain is located between the distal edge of the corrugated surface and the detachment fault breakaway, and consists of a morphologically complex area likely resulting from mass-wasting of the footwall cut off scarp at the initiation of the detachment fault (Escartín et al., 2017).

We identify and digitize individual corrugations on the exposed footwall of each OCC using bathymetric relief maps, calculated by applying a 200 m wide Gaussian filter in the slip-normal direction, which removes the overall domal morphology and reveals corrugations (Supplementary Figure 1). Individual corrugations, visually interpreted in map view, are shown in Figure 5.

Corrugations are evident on the exposed fault surfaces, and are also often visible axis-ward of the hanging-wall cutoff, indicating that the hanging wall apron is thin enough to reflect the prominent surface morphology of the underlying detachment fault (Figure 5). The appearance of corrugations on the apron also suggests that the apron is relatively thin, draping over the fault surface prior to its emergence at the seafloor, and revealing the underlying corrugations. Corrugations show a consistent alignment at each study site, typically within \pm 5° of the mean plate spreading direction (Supplementary Figure 2). This consistency implies that the process that governs corrugation azimuth is relatively constant and linked to the extension along the fault, and thus corrugation azimuth is a useful kinematic indicator. Corrugations often have well-defined end-points (Figure 4 and Supplementary Figure 1), indicating that they are discrete features with limited spatial (and thus probably temporal) extent in the displacement-parallel direction.

3.2 Corrugation geometry

The bathymetric data presented here allow us to assess the meter-scale geometry of corrugations at the five study sites. We quantify corrugation geometry in terms of spacing between corrugations, length along the spreading direction, width perpendicular to the spreading direction, and aspect ratio defined as length/width (Figure 6). The spreading-perpendicular distance between adjacent corrugations picked from relief maps (Supplementary Figure 1) is expressed as a probability density function, calculated using a kernel density estimation method (Figure 6a; Sheather and Jones, 1991). Corrugation length (measured parallel to slip) is plotted in Figure 6b, width perpendicular to slip is plotted in Figure 6d, and these two measurements are used to estimate aspect ratio, which is plotted in Figure 6d.

Corrugations are typically spaced 50 to 250 m apart, with a slight positive skew (i.e., higher number of corrugations spaced closer together) at all five sites. This spacing agrees well with that of lineations identified using near-bottom towed sidescan images at Atlantis Massif and 13°N on the MAR (Cann et al., 1997; MacLeod et al., 2009), and at the FUJI dome on the Southwest Indian Ridge (Searle et al., 2003).

Corrugations at SCC are most commonly spaced at ~100 m. This is a slightly larger spacing than that observed at the other four sites, which are commonly spaced at ~60 m (Figure 6a). Corrugations appear to be discrete in length, i.e. do not extend across the entire exposed fault surface. Lengths vary between tens of meters to ~1500 m, and are mostly 100-500 m long across all sites (Figure 6b), although these length estimates probably represent lower bounds. Mass-wasting products may cover up corrugation ends at the chaotic terrain boundary (Figure 5), while some corrugations may only be partially exposed from beneath the hanging wall apron at the axial-side of the fault surface. Corrugations range in width between 20 and 100 m, with a positive skew at all sites, which reflects that most corrugations are 20-50 m wide (Figure 6c). These measurements at the fault surface reveal that the aspect ratio of corrugations is typically ~10:1, but can be as high as ~50:1 in a few cases (Figure 6d). Given that the full length of some corrugations may be partly obscured (by mass wasting or hydrothermal deposits, for example), these estimates of aspect ratio also represent lower bounds.

3.3. Power spectral analysis

A useful measure of corrugation geometry, and of fault roughness, is power spectral density, where higher spectral density implies increased roughness for a given wavelength (Power et al., 1988; Power and Tullis, 1991). We extracted bathymetric profiles spaced 50 m apart and oriented parallel and perpendicular to slip from patches of exposed fault surface at each study location (Figure 7). We then calculated power spectral density curves for individual profiles using Thomson's multitaper method (Thomson, 1982), and summed the spectra together to give single spectra for each direction at each site (Figure 8). At wavelengths below ~10 m, spectra are contaminated by acquisition artifacts. These artifacts arise from vehicle attitude noise (heading, pitch and roll), from navigation errors generated as adjacent swaths are stitched together, and from gridding artifacts when overlapping swaths are merged. Variations in these errors occur both within and between surveys, and cannot be completely removed from the data. At wavelengths of 10 to 250 m, the power spectral density for each of the four corrugated surfaces is similar, reflecting a common level of roughness. The power spectral density function G(t) for the special case of a profile across a surface obeying a fractal scaling law is

$$G(f) = Cf^{-\beta} \tag{1}$$

where f is the spatial frequency, C is a constant, and β is the slope of the power spectrum (Brown, 1987), and describes how the surface roughness varies with scale. If the power-law relationship between length scale and roughness is well-fitted over several orders of magnitude, then the fault surface is fractal (e.g. Malamud and Turcotte, 1999); the special case of a well-fitted surface with $\beta = 3$, is said to be self-similar (e.g. Brown, 1987; Candela and Renard, 2012). If a surface is self-similar, a small portion of the surface, when magnified isotropically, will appear statistically identical to the entire surface. If a surface is self-affine, a magnified portion of the surface will only appear statistically identical to the entire surface if different magnifications are used for the directions parallel and perpendicular to the surface (e.g. Power and Tullis, 1991). Although slipparallel spectra from SCC, 13°30'N and 13°20 are well-fitted with $\beta = 3$ at wavelengths of 10–100 m, the power law does not fit over several orders of magnitude at any of the study sites, suggesting that fault surface roughness is not fractal (Figure 8).

296 Changes in fault surface roughness with increasing slip in terrestrial settings have been 297 interpreted to imply that the nucleation, growth, and termination of earthquakes on well-298 established faults are different to that on new ones (e.g. Sagy et al., 2007). Here, we apply 299 the roughness analysis to investigate whether the rupture process varies as a function of 300 slip on oceanic detachment faults. We restrict our analysis to the 13°20'N OCC, which 301 has the largest exposed fault surface area. We calculated power spectra for profiles in 302 three adjacent patches of fault surface, which have experienced 1.3, 2.6 and 3.9 km of 303 slip, respectively, since the fault surface emerged on the seafloor (see boxes 1, 2 and 3 in 304 Figure 9a inset). A comparison of spectra from these three patches shows that they all 305 have a similar level of fault roughness (Figure 9a), implying no variation in fault rupture 306 processes as a function of slip. At a larger scale, slip on the five oceanic detachment fault 307 surfaces analyzed here ranges from ~5 km at TAG to ~8 km at 13°20'N, however no 308 significant differences in slip-parallel fault roughness are apparent (Figure 8). Hence, 309 both within a single detachment surface, and between faults with different slip histories, 310 there does not appear to be variation in fault roughness with slip. We also calculated 311 roughness for profiles from a series of fault patches oriented perpendicular to slip at 312 13°20'N (see boxes 4, 5 and 6 in Figure 9b inset). We also find no significant variation in 313 roughness between these patches, implying that, at least for the exposed portion of the 314 fault, the rupture process is fairly uniform along strike (i.e. parallel to the spreading axis). 315 These results imply that the process of corrugation nucleation and development is 316 relatively stable throughout the duration of slip on oceanic detachment faults.

317

318

319

320

321

295

4. Corrugated fault formation

The geometric analysis of corrugations based on near-bottom data presented here provides an opportunity to address the ongoing debate about the origin of detachment fault corrugations. Here we compare and evaluate three competing hypotheses for corrugation development.

322323

324

4.1 Continuous casting

325326

327

In the continuous casting hypothesis, footwall rocks below the detachment fault are suggested to be much weaker than those above the fault, and are molded to conform to

the irregular underside of the upper plate during normal fault movement that eventually led to exhumation of the corrugations (Spencer, 1999). Hence a corrugated pattern is thought to be imprinted onto the upper surface of the more ductile footwall material and to be preserved as the fault continues to slip. Three-dimensional observations of exposed oceanic detachment fault surfaces have shown that corrugations persist beneath the exposed fault surface, and occur in repeated layers within a zone that may be hundreds of meters thick (Bonnemains et al., 2017; Escartín et al., 2017). These findings show that the process of corrugation formation cannot be restricted to the interface between hanging wall and footwall, and must occur over a finite thickness in three dimensions. It is therefore unlikely to be explained by continuous casting, which would only generate corrugations on a single, two-dimensional planar surface. The observed finite corrugation length, with well-defined ends (e.g. Figure 4), is also not predicted by the continuous casting hypothesis, unless the shape of the brittle layer changed over time. The contrast in ductility between hanging wall and footwall would be required to abruptly dissipate and re-appear over very short timescales (thousands of years) in order to form corrugations that are a few hundreds of meters long, requiring an additional mechanism that seems physically improbable.

4.2 Uneven brittle-ductile transition depth

Tucholke et al., (2008), suggested that episodic, spatially variable magmatism may explain corrugations spaced hundreds of meters apart, in a modified version of the continuous casting hypothesis. Since intrusion of magma along the spreading center is thought to be discontinuous, Tucholke et al., (2008) envision an uneven brittle-plastic transition that would lead to depth-dependent fault initiation and thus the development of corrugations. In their model, the relatively cool hanging-wall would continue to control the shape of the exhuming footwall, with or without further magmatic injection, in a similar fashion to the continuous casting mechanism. In this hypothesis, the wavelength (i.e. spacing) of corrugations must depend upon the length scale of slip-perpendicular (i.e. spreading axis-parallel) rheological heterogeneities within the hanging wall. Such variations in rheology could either be due to variations in melt supply leading to thermal anomalies (Tucholke et al., 2008), or due to variations in the depth extent of serpentinization by seawater. Corrugations are commonly found on oceanic detachment

fault surfaces, however the extent of serpentinization varies between sites. For example, at the corrugated central dome of Atlantis Massif, drilling at site U1309 revealed that intense serpentinization in the upper ~100 m (Blackman et al., 2011), however samples from the corrugated surface at the 13°20N OCC are primarily quartz-cemented basaltic breccias (Bonnemains et al., 2017). Therefore, serpentinization alone is unlikely to cause the required rheological contrast, as it is not common to all detachments studied here. If this rheological contrast were caused by temperature anomalies within the hanging wall, the thermal contrast would need to be sustained for sufficient time for corrugations to form. A typical corrugation observed in AUV data here is 200-500 m in length (Figure 6a), and assuming a half spreading rate of ~10 km Ma⁻¹, the thermal contrast would need to be sustained for $\tau_C = 0.2-0.5$ Ma. Unless it is maintained by a steady, irregular pattern of upward heat advection along the axis, a thermal anomaly of wavelength λ at the brittle-ductile transition will diffuse over a characteristic time scale $\tau = \lambda^2 / \kappa$, where κ denotes the thermal diffusivity of the oceanic lithosphere (~3×10⁻⁶ m² s⁻¹; Turcotte and Schubert, 2002). Thus, only thermal anomalies of wavelengths greater than $\lambda_C = \sqrt{\kappa \tau_C} =$ 4–7 km can be sustained over sufficiently long time to mold a typical corrugation.

Since corrugations are typically spaced ~ 100 m apart or less (Figure 6a), it is unlikely that the necessary thermal contrast within the hanging wall could be sustained for a sufficient amount of time. A thermal anomaly with $\lambda = 100$ m, which would explain the typical spacing of corrugations observed in near-bottom multibeam data here and in shipboard multibeam data elsewhere, would dissipate within ~ 100 years. At a nominal half spreading rate of 10 km Ma⁻¹, such a thermal anomaly could only generate a corrugation that is ~ 1 m long, which is two orders of magnitude smaller than observed corrugation lengths (Figure 6b).

Alternatively, a thermal anomaly could be maintained by steady-state advection of heat into the same patch of the ridge axis during the time required to form a corrugation, thus generating a depth-varying brittle-ductile transition. This scenario is implausible for three reasons: First, there is no geological observation consistent with this type of behavior; second, there is no straightforward mechanism for maintaining such thermal anomalies over the necessary period of 0.2–0.5 Ma; third there is no evidence for thermal anomalies with such regular, close spacing at the ridge axis, as would be required. These simple

scaling arguments, combined with the detailed observations and sampling of corrugated surfaces and samples from the fault zone, demonstrate that variations in the brittle-ductile transition cannot explain corrugations on the scales observed at oceanic detachment faults.

398399

394

395

396

397

4.3 Strain localization along anastomosing faults

400

401

402

403

404

405

406

407

408

409

410

411

412

413

414

415

416

417

418

419

420

An alternative explanation for corrugation genesis on oceanic detachments involves strain localization within an anastomosing three-dimensional network of fault segments (Escartín et al., 2017). A fault structure reminiscent of an anastomosing ductile shear zone, exposed structurally beneath the projection of the detachment surface, has also been proposed for the Atlantis Massif OCC (Karson et al., 2006). Many normal faults on the continents are corrugated, and are thought to form by various mechanisms including reactivation of pre-existing faults and fractures, or progressive breakthrough of originally segmented (i.e. en echelon) fault networks (e.g. Ferrill et al., 1999; Jackson and McKenzie, 1999). In this model, small, individual rupture segments propagate laterally until they overlap, and fault tips eventually propagate along curved paths to intersect and link up with adjacent en echelon fault segments (Candela and Renard, 2012; Childs et al., 1995; Peacock, 2002). The resulting network of linked fault segments generates an overall scallop-shaped fault surface, with cuspate ridges that correspond to fault segment intersections (Ferrill et al., 1999). This process of fault segment linkage occurs in three dimensions. In the cross-fault direction, the network of slip planes occupies a finite thickness and is strongly layered. Intersections between slip planes delineate phacoidal blocks that are highly elongated in the direction of extension and show a range of alongstrike dimensions (Figure 10). When this complex detachment zone becomes exposed at the seafloor, the well-preserved phacoidal blocks imprint a subtle topography on the core complex dome, with amplitudes <10 m and wavelengths 1–100 m (Figure 7).

421

422

423

424

425

426

This model can be tested against a number of key observations. First, the occurrence of corrugations with wavelengths ranging from centimeters to hundreds of meters (Figures 1 and 6) can be explained by linkage of fault segments over a spectrum of length scales, without the requirement for *ad-hoc* small-scale rheological heterogeneities. Since corrugated faults are also found in continental settings, where rheological contrasts

cannot be explained by magmatism or serpentinization (although lithology and hydration contrasts may play a role), this hypothesis is applicable to fault surfaces in a wide range of settings.

Recent seismic reflection images have revealed corrugations along the Costa Rica subduction zone megathrust (Edwards et al., 2018). These corrugations are observed to initiate within hundreds of meters of the up-dip extent of the megathrust and extend down-dip to ~1.4 km below seafloor, with lengths of ~4-6 km measured along the fault plane. Corrugations are spaced ~200 m apart and extend 1 km or more, and considering the limited ability of seismic reflection images to resolve these structures, are comparable in scale to those at OCCs presented here. Hence despite subduction zone rocks presumably not having significant pre-existing ductile deformation fabrics (as expected at OCCs), they can still give rise to corrugations. The mechanism of strain localization leading to corrugated detachment surfaces may therefore apply to other environments such as subduction megathrusts, further suggesting that corrugation development may be a common by-product of brittle strain localization that is largely insensitive to lithology and deformation history. Corrugations on oceanic detachment faults therefore may not reflect a unique deformational process, but instead a greater propensity to preserve pristine fault surfaces. This enhanced preservation is due to the relative inefficiency of erosion inferred for young oceanic crust near spreading centers (Olive et al., 2017).

5. Implications for brittle processes during detachment fault growth

If OCC corrugations do reflect a complex mode of strain localization through interwoven fault segments, it is likely that the resulting phacoidal texture develops over a finite thickness interval within the fault zone, i.e., within a finite depth range below the seafloor. We refer to this portion of the fault as the corrugation factory, to highlight the idea that fault materials enter this zone with pre-existing ductile fabrics (e.g. foliations and lineations) or loosely connected crack networks, and emerge from it with a fully-developed anastomosed structure (Figure 10). We speculate that pre-existing ductile fabrics may influence the final anastomosed fault character, however since corrugations are present in continental faults and in subduction zones where ductile deformation is

unlikely or of limited importance, pre-existing fabrics may not be a requirement. The corrugation factory must lie within the brittle portion of the oceanic lithosphere, which corresponds to temperatures below ~600°C (Hirth et al., 1998). Microearthquakes, a manifestation of active brittle deformation, are known to occur down to depths of ~10 km near oceanic detachment faults (DeMartin et al., 2007; Parnell-Turner et al., 2017). This observation provides a plausible down-dip limit for the onset of corrugation formation.

466467

468

469

470

471

472

473

474

475

476

477

478

479

480

481

482

483

484

485

486

460

461

462

463

464

465

Morphological considerations, however, can help place more stringent constraints on the location of the corrugation factory along active detachment fault systems. In the case of the 13°20'N OCC, spectral analysis reveals no significant change in corrugated seafloor texture along the direction of extension within ~5 km of the hanging-wall cutoff (Figure 9a). In other words, increased slip on the detachment did not result in a significant change in roughness, which is contrary to reported interpretations from much shorter-offset continental normal faults (e.g., Sagy et al., 2007). Our findings suggest that the fault rocks exposed in the corrugated terrain have all experienced the same degree of strain, and thus acquired the same fabric. This hypothesis can be explained by a simple model illustrated in Figure 10d, which shows that the total strain accumulated within a shear zone of finite downdip extent, L, no longer depends on its accumulated offset once this offset exceeds L. Only fault rocks located close to the breakaway —which have not traveled through the entire extent of the corrugation factory— would show a gradient in recorded strain (and potentially fabric) in the slip direction (Figure 10d). At 13°20'N, such rocks may be located beneath the heavily mass-wasted terrain that lies within 5 to 9 km of the hanging-wall cutoff and would therefore be inaccessible to direct observation. However, since fault rocks located as close as ~4 km to the breakaway exhibit the same roughness as subsequently exposed fault rocks, the downdip extent of the corrugation factory could not have exceeded ~4 km, at least during the early stages for fault exhumation.

487

488

489

490

491

492

According to the fault geometry constrained by microseismicity and proposed by Parnell-Turner et al. (2017), the footwall rocks presently exposed at the 13°20'N hanging-wall cutoff likely originated at depths of ~8 km below seafloor. This means that the corrugation factory must lie at shallower levels, and also account for less than ~25% of the sub-seafloor extent of the detachment fault surface in the brittle domain. It is

therefore likely that corrugations originate within the uppermost ~4 km of the brittle domain. Interestingly, corrugations imaged on the Costa Rica megathrust are well developed at depths as shallow as ~1.4 km below seafloor (Edwards et al., 2018). This observation suggests that the strain accumulated by megathrust rocks at the initiation of burial (i.e., at low temperature and confining pressure) is sufficient to generate corrugations. At 13°20'N, the uppermost 4 km of the detachment does not presently host microearthquakes (Parnell-Turner et al., 2017), but may occasionally rupture during larger, teleseismically-detected events (Craig and Parnell-Turner, 2017). Strong microseismicity however occurs at depths of 4–6 km and 7–12 km below seafloor at the TAG and 13°20'N detachments, respectively (deMartin et al., 2007; Parnell-Turner et al., 2017). While the corrugation factory clearly could not have been situated at those depths when the 13°20'N detachment formed, it is possible that it has deepened through time, as the entire detachment system matured.

Detachment microearthquakes typically have local magnitudes (M_L) ranging between 0.5 and 1.5 (DeMartin et al., 2007; Parnell-Turner et al., 2017). Assuming that a fault patch can be approximated by a circular crack, the rupture area, a, associated with an earthquake can be written in terms of seismic moment, M_0 , as

$$511 a = \sqrt[3]{\frac{7}{16} \frac{M_0}{\Delta \sigma}}, (2)$$

where $\Delta \sigma$ is stress drop (assumed to be 3 MPa), and M_0 is related to M_L by

$$\log_{10} M_0 = 1.5 M_L + 16.1. \tag{\varepsilon}$$

Microearthquakes with typical M_L ranging between 0.5 and 1.5 would therefore be expected to occur on rupture patches 20–30 m² in area, or 5–6 m in diameter. This characteristic rupture diameter is smaller than the areal extent of individual corrugations revealed by the microbathymetric data. We therefore propose that the microearthquake activity represents the breaking of new slip planes (below 4 km beneath the seafloor) that will eventually coalesce at shallower depths (above 4 km) within the corrugation factory to form the final anastomosing fabric, which includes structures on length scales from centimeters to hundreds of meters. We thus speculate that the corrugation factory in the

active 13°20'N and TAG detachments must have been at depths < 4 km during the early stages of fault slip. Its modern-day depth window may begin as shallow as \sim 2 km based on geological sampling (Bonnemains et al., 2016), and may also now overlap with the depth extent of microearthquakes at depths > 4 km (Parnell-Turner et al., 2017).

6. Conclusions

We have compiled and analyzed 2 m resolution near-bottom bathymetric data acquired by AUV over five corrugated oceanic detachment fault surfaces along the Mid-Atlantic Ridge. Despite having variable footwall lithology and recording different amounts of slip, we find that the geometry of corrugations at the five sites is remarkably consistent: spacing is typically 50–250 m, and slip-parallel lengths are mostly 100–500 m for example. We also find that corrugations have well-defined ends, and do not extend across the entire exposed fault surface. Spectral analysis shows that fault surfaces at the five sites have comparable levels of roughness, and are not self-similar or self-affine. We find that fault roughness does not vary as a function of slip, implying that for the portion of fault surfaces observed here, the process of fault nucleation and growth is relatively constant as extension proceeds. This result is in contrast to findings for terrestrial normal faults, probably because the surfaces that record the comparable early stages of slip at oceanic detachments studied here are hidden beneath the breakaway zone.

We have used our observations to evaluate three hypotheses for corrugation genesis. The continuous casting hypothesis is inconsistent with earlier seafloor observations of the three-dimensional character of the corrugated fault zone, which may be hundreds of meters thick (Bonnemains et al., 2017; Escartín et al., 2017). This hypothesis is also inconsistent with the observation that corrugations are finite in length, and therefore cannot be formed 'continuously'. We use simple thermal scaling arguments to show that the varying brittle-ductile depth hypothesis cannot explain the observed length and spacing of corrugations. We find that any thermally-driven rheological anomaly would dissipate long before a corrugation could form, unless unfeasibly high spreading rates are invoked.

We conclude that the strain localization hypothesis, where a network of small rupture patches coalesces into an uneven fault surface within a corrugation factory, best explains presence and geometry of corrugated fault surfaces on oceanic detachments. This corrugation factory likely initiated at depths shallower than ~4 km when the 13°20'N and TAG detachments first formed. It may now lie at depths closer to ~4 km and overlap with the microseismically-active portion of these faults, where new slip surfaces initiate before eventually coalescing over a few km along the fault. This hypothesis is not dependent upon thermal or rheological fault variability, nor on pre-existing deformation fabrics, and may thus be applicable to faults in terrestrial and subduction zone settings, where corrugations are also documented. Hence fracture linkage and displacement can lead to corrugations on fault surfaces regardless of the setting.

Acknowledgements

Near-bottom bathymetric data acquisition was supported by National Science Foundation (NSF) grant OCE-1155650, GEOMAR, CNRS, IFREMER, and INSU. Mapping at TAG was supported by Project 604500 "Blue Mining" under the EU 7th Framework Programme. RPT was supported by NSF grant OCE-1736547. We thank the crew and science parties of RV *Knorr*, RV *Meteor* and N/O *Pourquoi Pas?*, and the engineering teams of AUVs *Abyss* and *Sentry* for their hard work and professionalism. We are grateful for the detailed and constructive comments from two anonymous reviewers. Data from KN210-05 and ODEMAR cruises are available at doi:10.7284/900548 and doi:10.17600/13030070, respectively.

581	
582	References
583	
584	Blackman, D.K., Ildefonse, B., John, B.E., Ohara, Y., Miller, D.J., Abe, N., Abratis, M.,
585	Andal, E.S., Andreani, M., Awaji, S., Beard, J.S., Brunelli, D., Charney, A.B.,
586	Christie, D.M., Collins, J.A., Delacour, A.G., Delius, H., Drouin, M., Einaudi, F.,
587	Escartín, J., Frost, B.R., Green, G.F., Fryer, P.B., Gee, J.S., Godard, M., Grimes,
588	C.B., Halfpenny, A., Hansen, H.E., Harris, A.C., Tamura, A., Hayman, N.,
589	Hellebrand, E., Hirose, T., Hirth, G., Ishimaru, S., Johnson, K.T.M., Karner, G.D.,
590	Linek, M., MacLeod, C.J., Maeda, J., Mason, O.U., McCaig, A.M., Michibayashi,
591	K., Morris, A., Nakagawa, T., Nozaka, T., Rosner, M., Searle, R.C., Suhr, G.,
592	Tominaga, M., von der Handt, A., Yamasaki, T., Zhao, X., 2011. Drilling
593	constraints on lithospheric accretion and evolution at Atlantis Massif, Mid-Atlantic
594	Ridge 30°N. J. Geophys. Res. 116. doi:10.1029/2010JB007931
595	Bonnemains, D., Escartín, J., Mével, C., Andreani, M., Verlaguet, A., 2017. Pervasive
596	silicification and hangingwall overplating along the 13°20' N oceanic detachment
597	fault (Mid-Atlantic Ridge). Geochem. Geophys. Geosyst 18, 2028–2053.
598	doi:10.1002/2017GC006846
599	Bonnemains, D., Verlaguet, A., Escartín, J., Mevel, C., Andreani, M., 2016.
600	Hydrothermal circulation along oceanic detachment fault: Constraints on the nature
601	and conditions of syntectonic silicification at the 13°20'N oceanic core complex
602	(Mid-Atlantic ridge). Abstr. T33A-3001 Present. 2016 Fall Meet. AGU, San Fr.
603	Calif. 12-16 Dec.
604	Brown, S.R., 1987. A note on the description of surface roughness using fractal
605	dimension. Geophys. Res. Lett. 14, 1095-1098. doi:10.1029/GL014i011p01095
606	Candela, T., Renard, F., 2012. Segment linkage process at the origin of slip surface
607	roughness: Evidence from the Dixie Valley fault. J. Struct. Geol. 45, 87-100.
608	doi:10.1016/j.jsg.2012.06.003
609	Cann, J.R., Blackman, D.K., Smith, D.K., McAllister, E., Janssen, B., Mello, S.,
610	Avgerinos, E., Pascoe, A.R., Escartín, J., 1997. Corrugated slip surfaces formed at
611	ridge-transform intersections on the Mid-Atlantic Ridge. Nature 385, 329-332.
612	Childs, C., Watterson, J., Walsh, J.J., 1995. Fault overlap zones within developing
613	normal fault systems. J. Geol. Soc. 152, 535-549.

- 614 Craig, T.J., Parnell-Turner, R., 2017. Depth-varying seismogenesis on an oceanic
- detachment fault at 13°20'N on the Mid-Atlantic Ridge. Earth Planet. Sci. Lett. 479,
- 616 60–70. doi:10.1016/j.epsl.2015.01.026
- DeMartin, B.J., Sohn, R.A., Canales, J.P., Humphris, S.E., 2007. Kinematics and
- geometry of active detachment faulting beneath the Trans-Atlantic Geotraverse
- 619 (TAG) hydrothermal field on the Mid-Atlantic Ridge. Geology 35, 711–714.
- doi:10.1130/G23718A.1
- 621 Edwards, J.H., Kluesner, J.W., Silver, E.A., Brodsky, E.E., Brothers, D.S., Bangs, N.L.,
- Kirkpatrick, J.D., Wood, R., Okamoto, K., 2018. Corrugated megathrust revealed
- offshore from Costa Rica. Nat. Geosci. 11, 197–202. doi:10.1038/s41561-018-0061-
- 624 4
- 625 Escartín, J., Canales, J.P., 2011. Detachments in oceanic lithosphere: Deformation,
- magmatism, fluid flow, and ecosystems. Eos Trans., AGU 92, 31.
- 627 Escartín, J., Petersen, S., Bonnemains, D., Cannat, M., Andreani, M., Bezos, A.,
- Chavagnac, V., Choi, Y., Godard, M., Haaga, K., Hamelin, C., Ildefonse, B.,
- Jamieson, J., John, B.E., Leleu, T., MacLeod, C.J., Massot-Campos, M., Nomikou,
- P., Olive, J.A., Paquet, M., Rommevaux, C., Rothenbeck, M., Steinfuhrer, A.,
- Tominaga, M., Triebe, L., Garcia, R., Campos, R., 2017. Tectonic structure,
- evolution, and the nature of oceanic core complexes and their detachment fault
- zones (13°20' N and 13°30'N, Mid Atlantic Ridge). Geochem. Geophys. Geosyst
- 634 18. doi:10.1002/2016GC006775
- Escartín, J., Smith, D.K., Cann, J.R., Schouten, H., Langmuir, C.H., Escrig, S., 2008.
- 636 Central role of detachment faults in accretion of slow-spreading oceanic lithosphere.
- Nature 455, 790–794. doi:10.1038/nature07333
- 638 Ferrill, D.A., Stamatakos, J.A., Sims, D., 1999. Normal fault corrugation: implications
- for growth and seismicity of active normal faults. J. Struct. Geol. 21, 1027–1038.
- doi:10.1016/S0191-8141(99)00017-6
- Fletcher, J.M., Bartley, J.M., 1994. Constrictional strain in a non-coaxial shear zone:
- implications for fold and rock fabric development, central Mojave metamorphic core
- 643 complex, California. J. Struct. Geol. 16, 555–570. doi:10.1016/0191-
- 644 8141(94)90097-3
- Hirth, G., Escartín, J., Lin, J., 1998. The Rheology of the Lower Oceanic Crust:
- Implications for Lithospheric Deformation at Mid-Ocean Ridges, in: Faulting and

- Magmatism at Mid-Ocean Ridges, Geophysical Monograph 106. American
- Geophysical Union, pp. 291–303. doi:10.1029/GM106p0291
- Jackson, J., McKenzie, D.P., 1999. A hectare of fresh striations on the Arkitsa Fault,
- 650 central Greece. J. Struct. Geol. 21, 1–6. doi:10.1016/S0191-8141(98)00091-1
- John, B.E., 1987. Geometry and evolution of a mid-crustal extensional fault system:
- Chemehuevi Mountains, southeastern California. Geol. Soc. Spec. Pub. 313–335.
- doi:10.1144/GSL.SP.1987.028.01.20
- Karson, J.A., 1999. Geological investigation of a lineated massif at the Kane Transform
- Fault: implications for oceanic core complexes. Philos. Trans. R. Soc. Lond. A 357,
- 656 713–736. doi:10.1098/rsta.1999.0350
- Karson, J.A., Dick, H.J.B., 1983. Tectonics of ridge-transform intersections at the Kane
- fracture zone. Mar. Geophys. Res. 6, 51–98. doi:10.1007/BF00300398
- Karson, J.A., Früh-Green, G., Kelley, D.S., Williams, E.A., Yoerger, D., Jakuba, M.,
- 2006. Detachment shear zone of the Atlantis Massif core complex, Mid-Atlantic
- Ridge, 30°N. Geochem. Geophys. Geosyst 7. doi:10.1029/2005GC001109
- Karson, J.A., Rona, P.A., 1990. Block-tilting, transfer faults, and structural control of
- magmatic and hydrothermal processes in the TAG area, Mid-Atlantic Ridge 26°N.
- Geol. Soc. Am. Bull. 102, 1635–1645. doi:10.1130/0016-
- 665 7606(1990)102<1635:BTTFAS>2.3.CO;2
- Lalou, C., Reyss, J.-L., Brichet, E., Rona, P.A., Thompson, G., 1995. Hydrothermal
- activity on a 10⁵ -year scale at a slow spreading ridge, TAG hydrothermal field,
- Mid-Atlantic Ridge 26N. J. Geophys. Res. 100, 17,855-17,862.
- doi:10.1029/95jb01858
- MacLeod, C.J., Escartín, J., Banerji, D., Banks, G.J., Gleeson, M., Irving, D.H.B., Lilly,
- R.M., McCaig, A.M., Niu, Y., Allerton, S., Smith, D.K., 2002. Direct geological
- evidence for oceanic detachment faulting: The Mid-Atlantic Ridge, 15 45' N.
- 673 Geology 30, 879–882. doi:10.1130/0091-7613(2002)030<0879
- MacLeod, C.J., Searle, R.C., Murton, B.J., Casey, J.F., Mallows, C., Unsworth, S.C.,
- Achenbach, K.L., Harris, M., 2009. Life cycle of oceanic core complexes. Earth
- Planet. Sci. Lett. 287, 333–344. doi:10.1016/j.epsl.2009.08.016
- Malamud, B.D., Turcotte, D.L., 1999. Self-affine time series: 1. Generation and analyses.
- 678 Adv. Geophys. 40, 1–90.
- Mallows, C., Searle, R.C., 2012. A geophysical study of oceanic core complexes and

- surrounding terrain, Mid-Atlantic Ridge 13°N-14°N. Geochem. Geophys. Geosyst
- 681 13. doi:10.1130/G39232.1
- Olive, J.-A., Parnell-Turner, R., Escartín, J., Smith, D.K., Petersen, S., 2017. Controls on
- the Seafloor Exposure of Detachment Fault Surfaces. Abstr. T33D-0750 Present.
- 684 2017 Fall Meet. AGU, New Orleans, LA, 11-15 Dec.
- Parnell-Turner, R., Cann, J.R., Smith, D.K., Schouten, H., Yoerger, D., Palmiotto, C.,
- Zheleznov, A., Bai, H., 2014. Sedimentation rates test models of oceanic detachment
- faulting. Geophys. Res. Lett. 41. doi:10.1002/2014GL061555
- Parnell-Turner, R., Schouten, H., Smith, D.K., 2016. Tectonic Structure of the Mid-
- Atlantic Ridge near 16°30'N. Geochem. Geophys. Geosyst doi:
- 690 10.1002/2016GC006514.
- Parnell-Turner, R., Sohn, R.A., Peirce, C., Reston, T.J., Macleod, C.J., Searle, R.C.,
- Simão, N., 2017. Oceanic Detachment Faults Generate Compression in Extension.
- Geology 45, 932–926. doi:10.1130/G39232.1
- Peacock, D.C.P., 2002. Propagation, interaction and linkage in normal fault systems.
- Earth-Science Rev. 58, 121–142. doi:10.1016/S0012-8252(01)00085-X
- Power, W.L., Tullis, T.E., 1991. Euclidean and fractal models for the description of rock
- 697 surface roughness. J. Geophys. Res. 96, 415. doi:10.1029/90JB02107
- 698 Power, W.L., Tullis, T.E., Weeks, J.D., 1988. Roughness and wear during brittle faulting.
- J. Geophys. Res. 93, 15,268-15,278. doi:10.1029/JB093iB12p15268
- Rona, P.A., Hannington, M.D., Raman, C.V., Thompson, G., Tivey, M.K., Humphris,
- S.E., Lalou, C., Petersen, S., 1993. Active and relict sea-floor hydrothermal
- mineralization at the TAG hydrothermal field, Mid-Atlantic Ridge. Econ. Geol. 88,
- 703 1989–2017.
- Rona, P.A., Klinkhammer, G., Nelsen, T.A., Trefry, J.H., Elderfield, H., 1986. Black
- smokers, massive sulphides and vent biota at the Mid-Atlantic Ridge. Nature 321.
- 706 33–37. doi:10.1038/321033a0
- Sagy, A., Brodsky, E.E., Axen, G.J., 2007. Evolution of fault-surface roughness with slip.
- 708 Geology 35, 283–286. doi:10.1130/G23235A.1
- Schroeder, T., John, B.E., 2004. Strain localization on an oceanic detachment fault
- system, Atlantis Massif, 30°N, Mid-Atlantic Ridge. Geochem. Geophys. Geosyst 5.
- 711 doi:10.1029/2004GC000728
- Scott, R.B., Rona, P.A., McGregor, B.A., 1974. The TAG hydrothermal field. Nature

- 713 251, 301–302. doi:10.1038/252497a0
- Searle, R.C., Cannat, M., Fujioka, K., Mevel, C., Fujimoto, H., Bralee, A., Parson, L.,
- 715 2003. FUJI Dome: A large detachment fault near 64°E on the very slow-spreading
- southwest Indian Ridge. Geochem. Geophys. Geosyst 4.
- 717 doi:10.1029/2003GC000519
- Sheather, S.J., Jones, M.C., 1991. A Reliable Data-Based Bandwidth Selection Method
- for Kernel Density Estimation. J. R. Stat. Soc. B 53, 683–690.
- 720 Smith, D.K., Escartín, J., Schouten, H., Cann, J.R., 2008. Fault rotation and core complex
- formation: Significant processes in seafloor formation at slow-spreading mid-ocean
- ridges (Mid-Atlantic Ridge, 13°–15°N). Geochem. Geophys. Geosyst 9.
- 723 doi:10.1029/2007GC001699
- 724 Smith, D.K., Schouten, H., Dick, H.J.B., Cann, J.R., Salters, V., Marschall, H., Ji, F.,
- Yoerger, D., Sanfilippo, A., Parnell-Turner, R., Palmiotto, C., Zheleznov, A., Bai,
- H., Junkin, W., Urann, B., Dick, S., Sulanowska, M., Lemmond, P., Curry, S., 2014.
- Development and evolution of detachment faulting along 50 km of the Mid-Atlantic
- Ridge near 16.5°N. Geochem. Geophys. Geosyst 15, 4692–4711.
- 729 doi:10.1002/2014GC005563
- 730 Spencer, J.E., 1999. Geologic continuous casting below continental and deep-sea
- detachment faults and at the striated extrusion of Sacsayhuamán, Peru. Geology 27,
- 732 327–330. doi:10.1130/0091-7613(1999)027<0327
- 733 Thomson, D.J., 1982. Spectrum estimation and harmonic analysis. Proc. IEEE 70, 1055–
- 734 1096. doi:10.1109/PROC.1982.12433
- 735 Tivey, M.A., Schouten, H., Kleinrock, M.C., 2003. A near-bottom magnetic survey of the
- 736 Mid-Atlantic Ridge axis at 26°N: Implications for the tectonic evolution of the TAG
- 737 segment. J. Geophys. Res. 108, 1–13. doi:10.1029/2002JB001967
- 738 Tucholke, B.E., Behn, M.D., Buck, W.R., Lin, J., 2008. Role of melt supply in oceanic
- detachment faulting and formation of megamullions. Geology 36, 455.
- 740 doi:10.1130/G24639A.1
- 741 Tucholke, B.E., Lin, J., Kleinrock, M.C.C., 1998. Megamullions and mullion structure
- defining oceanic metamorphic core complexes on the Mid-Atlantic Ridge. J.
- 743 Geophys. Res. 103, 9857–9866.
- 744 Turcotte, D.L., Schubert, G., 2002. Geodynamics. Cambridge University Press.
- 745 doi:10.1017/CBO9780511807442

Whitney, D.L., Teyssier, C., Rey, P., Roger Buck, W., 2013. Continental and oceanic core complexes. Bull. Geol. Soc. Am. 125, 273–298. doi:10.1130/B30754.1
Zonenshain, L.P., Kuzmin, M.I., Lisitsin, A.P., Bogdanov, Y.A., Baranov, B. V., 1989.
Tectonics of the Mid-Atlantic rift valley between the TAG and MARK areas (26-24°N): Evidence for vertical tectonism. Tectonophysics 159, 1–23. doi:10.1016/0040-1951(89)90167-4
doi:10.1016/0040-1951(89)90167-4

Figures755

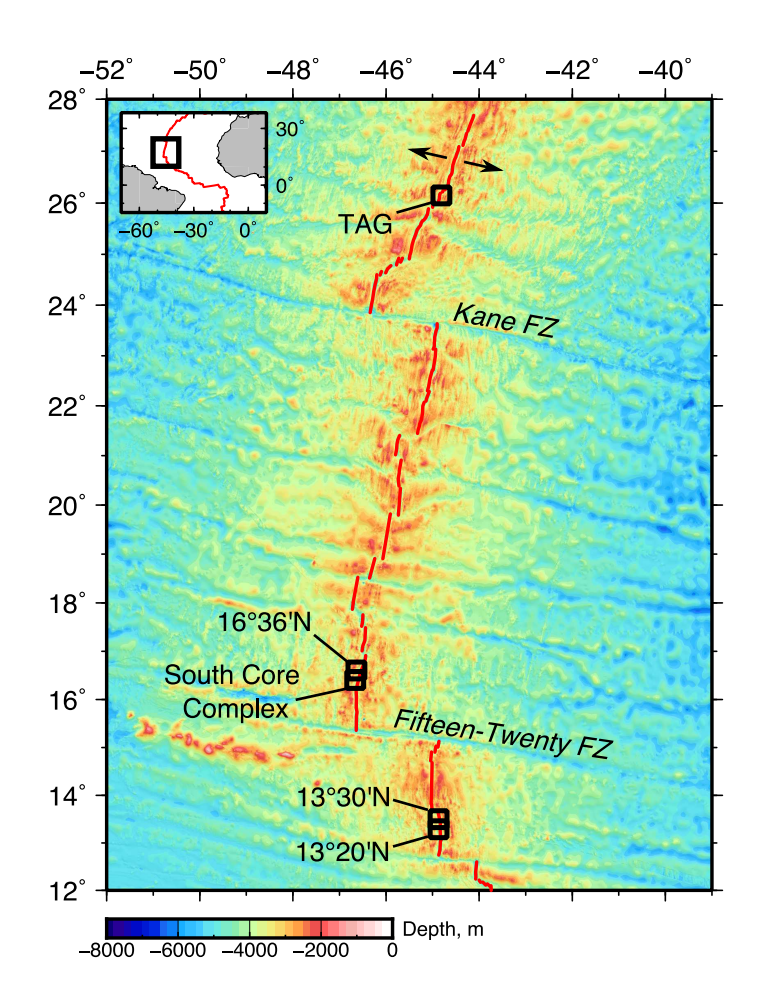


Figure 1. Location of five studied oceanic detachments along the northern Mid-Atlantic Ridge (black boxes), surveyed with near-bottom AUV dives; red line is ridge axis; arrows show spreading direction; selected fracture zones (FZ) labeled. Inset: black box shows location of main panel; red line is ridge axis.

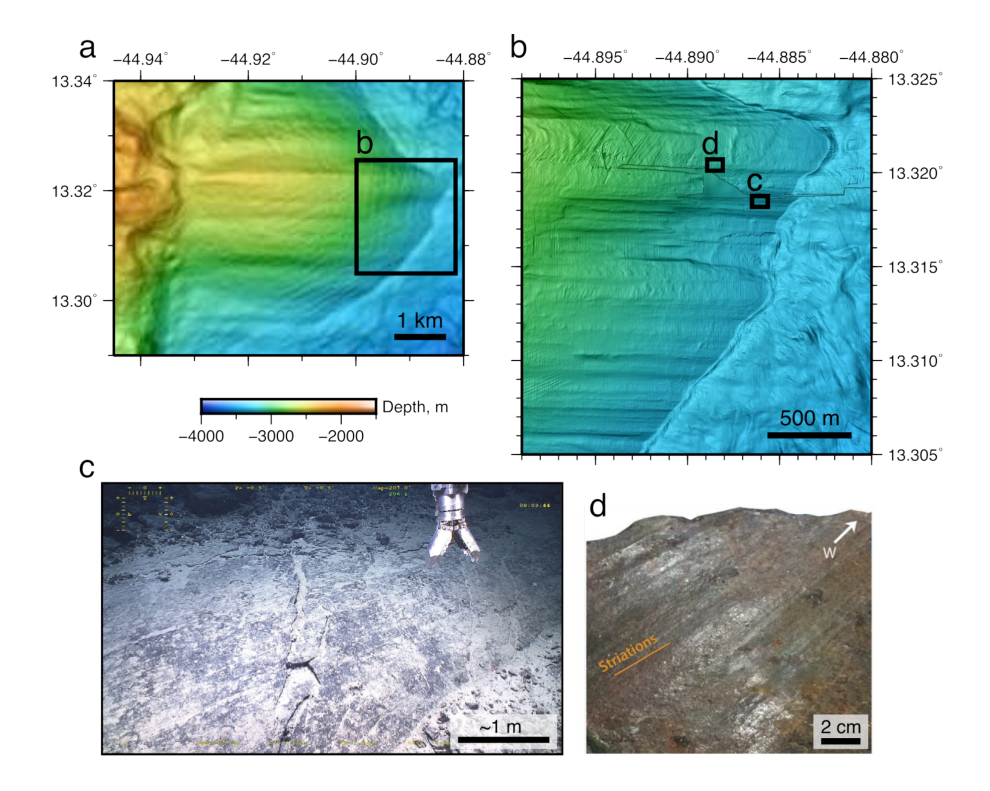


Figure 2. Corrugated fault surface imaged at kilometer to centimeter scales, at 13°20'N. a) Shipboard bathymetric data, gridded at 40 m node spacing (Escartín et al., 2017). Note corrugations on hundreds of meters scale, on top of larger kilometer-scale domed fault surface. b) Bathymetric data acquired near-bottom by AUV (Escartín et al., 2017), location shown in (a). Note corrugations visible at wavelengths of tens of meters. c) Seafloor image of striated fault surface (Escartín et al., 2017), location shown in (b), on flank of a bathymetric corrugation. Note that fault striations are spaced < 1 m apart, and are sub-horizontal, oriented parallel to displacement and to corrugations in (b). d) Macrophotograph of fault rock (sample ODM217), containing ultramafic clasts, showing cm- to mm-scale spreading-parallel striations (Bonnemains et al., 2017); sampling

location shown in (b).

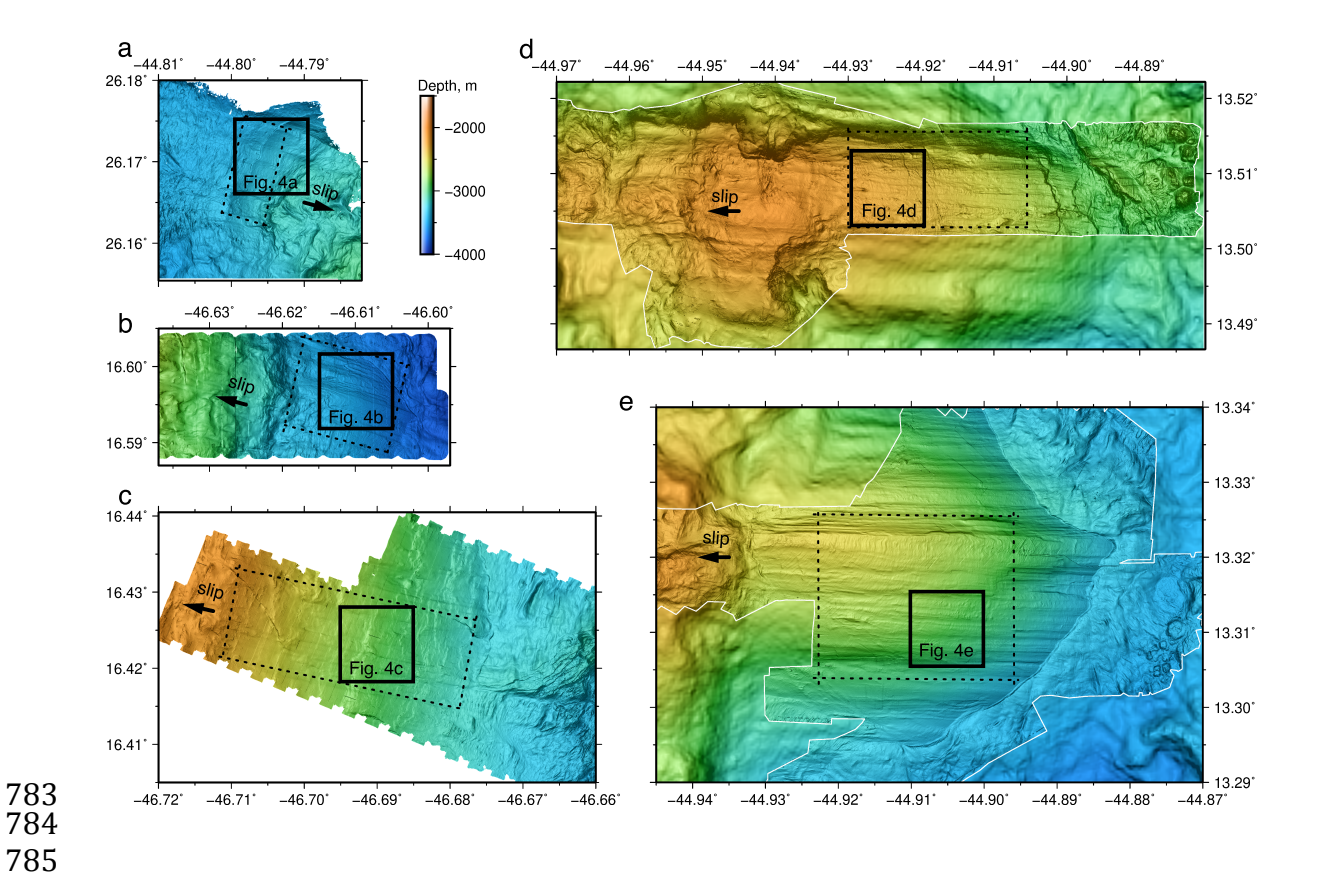


Figure 3. Near-bottom multibeam bathymetric surveys over corrugated detachment fault surfaces, acquired during AUV surveys. Data gridded at ~2 m grid cell size and maps plotted in Mercator projection at equal scale, with locations shown in Figure 1. a) TAG (this study). b) 16°36'N (Smith et al., 2014). c) SCC (Smith et al., 2014). d) and e) 13°30'N and 13°20'N (Escartín et al., 2017). Arrows show inferred slip direction; solid boxes locate panels in Figure 4; dashed boxes mark area of fault surfaces used to extract profiles and spectra (Figure 7); white lines in (d) and (e) mark AUV survey extents.

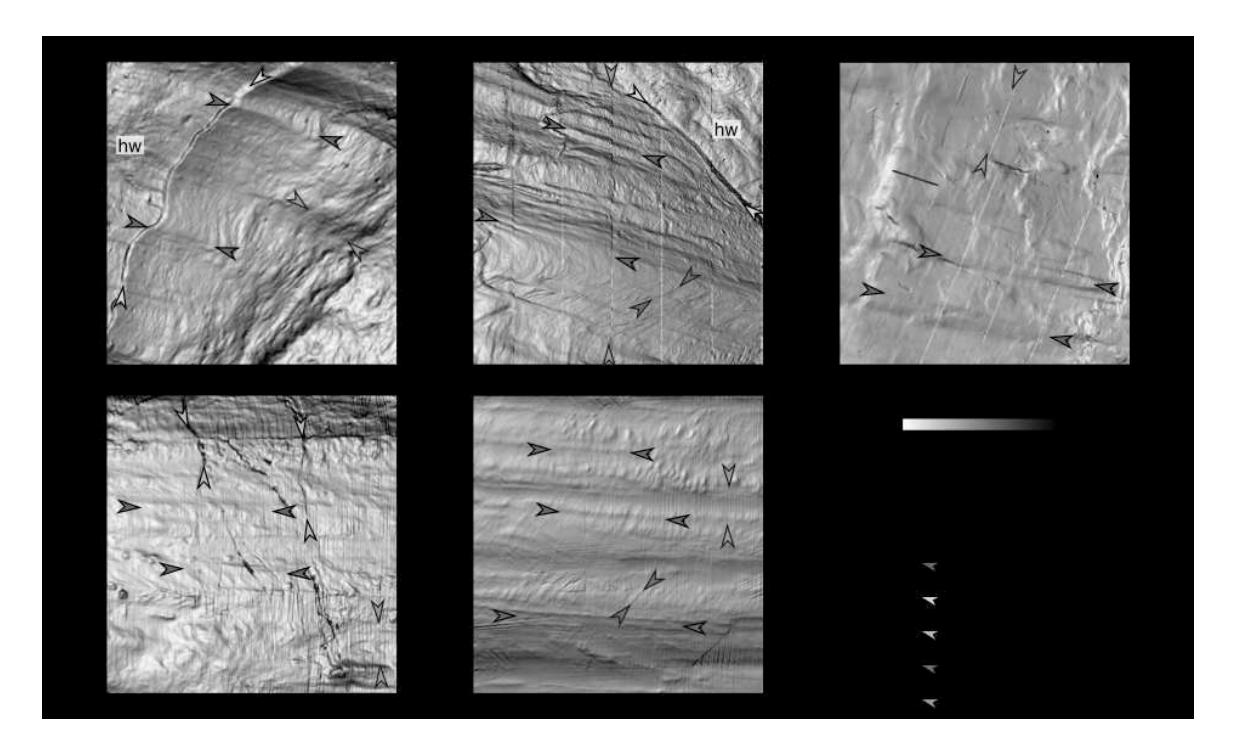


Figure 4. Detailed views of corrugated fault surfaces. Zooms of bathymetric slope plotted at equal scale, with arrows showing hanging-wall cutoff (yellow), corrugation highs (red), rubble ridges (blue), cross-cutting faults (green), and examples of artifacts (pink; note AUV roll artifacts spaced ~200 m apart in (a), (d) and (e), and >1 km-long artifacts along overlap between adjacent swaths in (b) and (c); zoom locations shown in Figure 3. Hanging wall (hw) is marked where visible. a) TAG. b) 16°36'N. c) SCC. d) 13°30'N. e) 13°20'N.

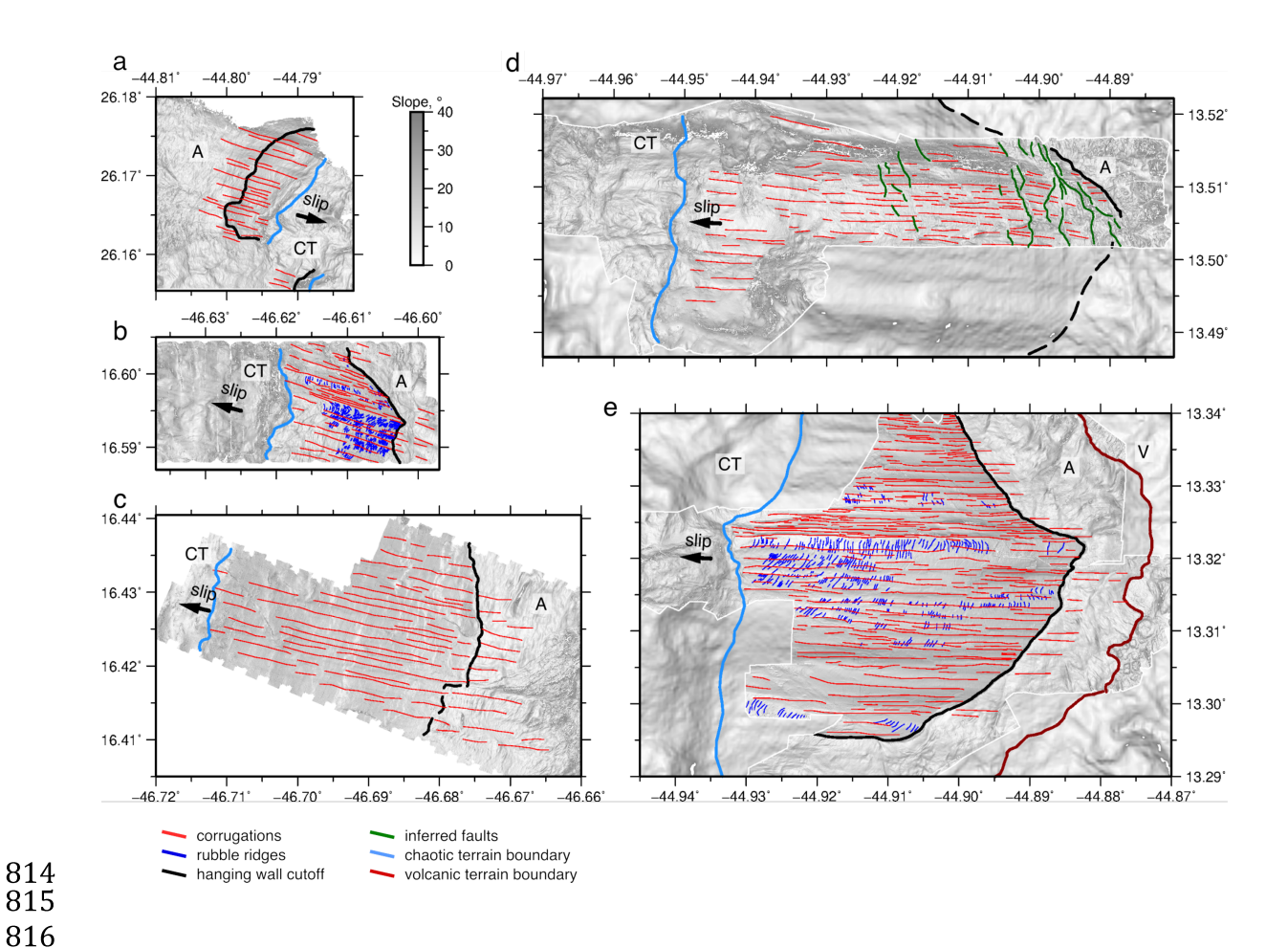


Figure 5. Bathymetric slope maps with interpretation of seafloor features. Red lines are interpreted spreading-parallel corrugations, based on linear relief identified in short-wavelength filtered maps (Supplementary Figure 1); short blue lines are rubble ridges lying on corrugated fault surface; black lines are the hanging-wall cutoff (dashed where uncertain); light blue line marks boundary between corrugated surface and chaotic terrain (CT); dark red line in (e) marks boundary between apron and volcanic terrain (V). Corrugated surfaces are bound on either side by chaotic terrain (CT) and apron (A). a) TAG. b) 16°36'N. c) SCC. d) 13°30'N. e) 13°20'N.

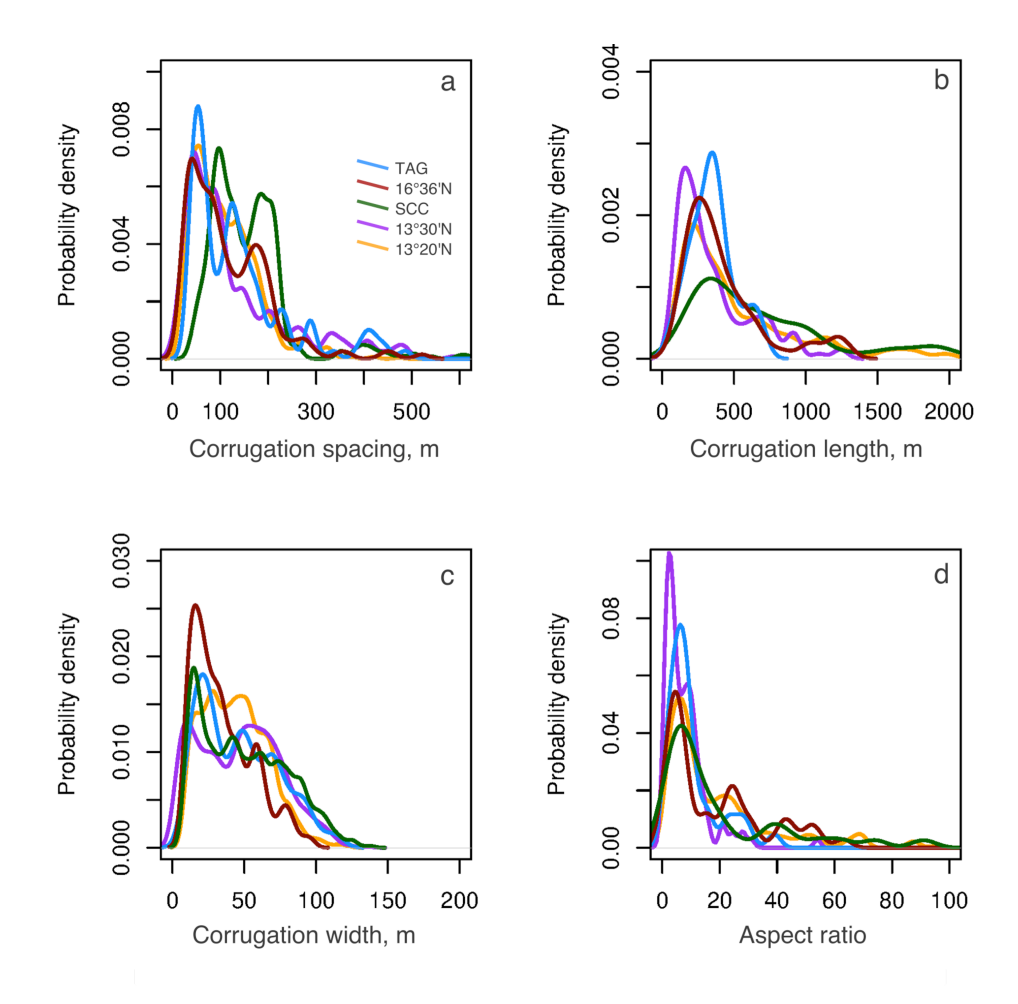


Figure 6. Fault surface corrugation statistics. a) Corrugation spacing. Probability density function obtained with kernel density estimation from interpreted corrugations shown in Figure 5; colors indicate location (see key). b) Corrugation length. c) Corrugation width. d) Corrugation aspect ratio defined as corrugation width/length.

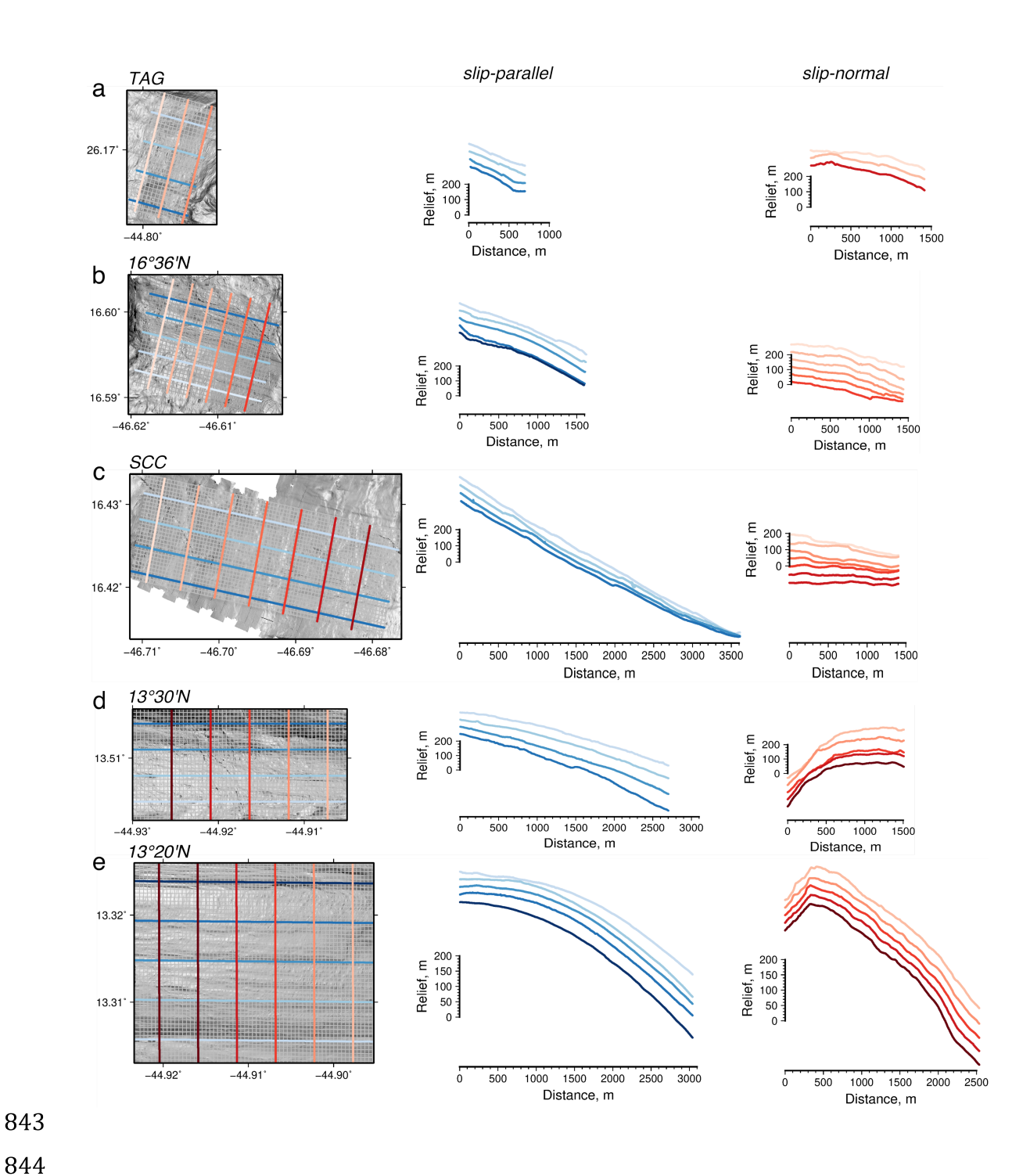


Figure 7. Bathymetric profiles used for spectral analysis. Left column are slope maps plotted at equal scale, location marked by dashed boxes in Figure 2; gray lines are location of all profiles at 50 m spacing; blue/red lines are selected slip-parallel and slip-normal profiles, respectively, shown in center and right columns. a) TAG. b) 16°36'N. c) SCC. d) 13°30'N. e) 13°20'N.

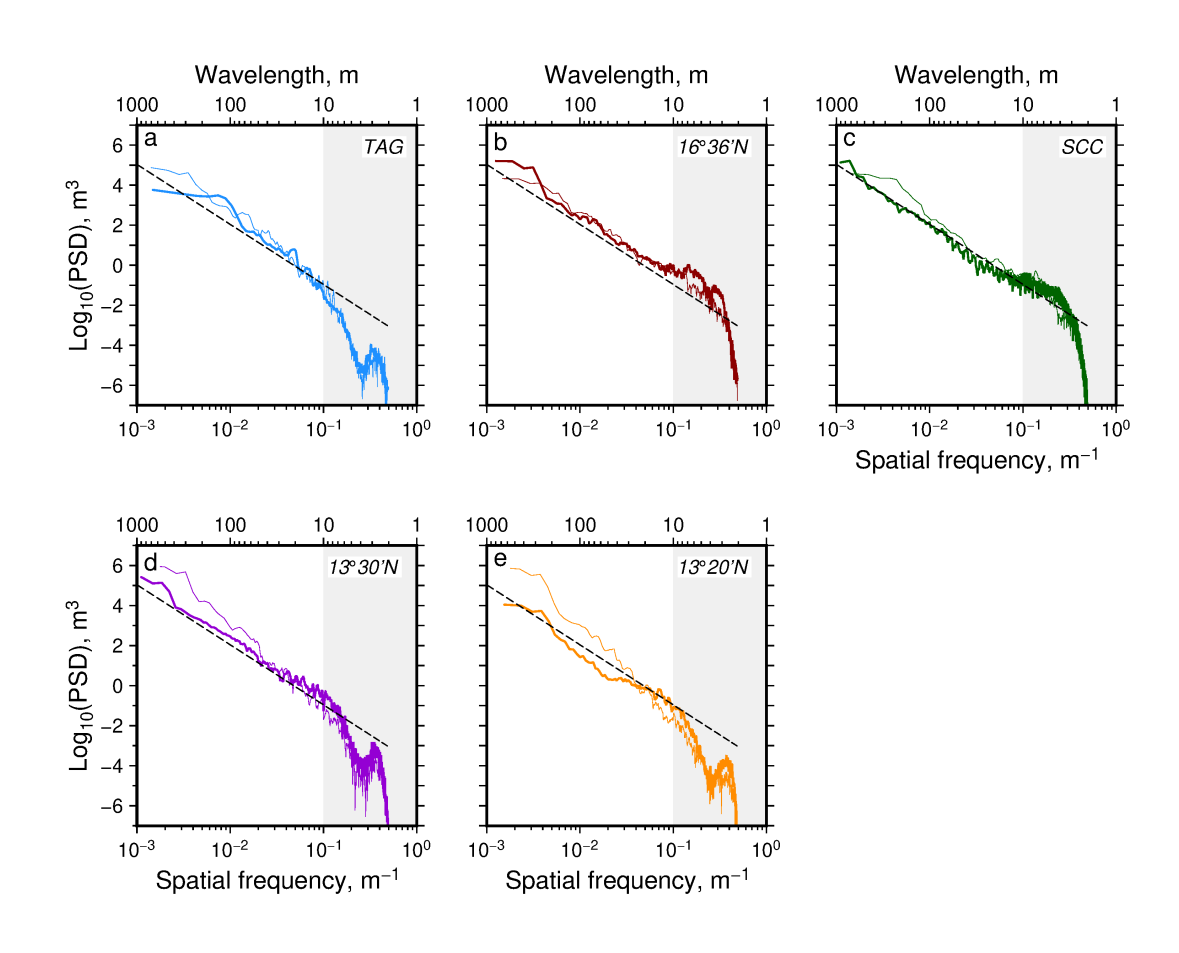


Figure 8. Power spectra. Power spectral density of bathymetric profiles from Figure 7; thick/thin lines are spectra from slip-parallel/normal profiles, respectively. Dashed line is slope of spectra of self-similar surface ($\beta = 3$), which is less than or equal to slope of observed spectra in most cases. a) TAG. b) 16°36'N. c) SCC. d) 13°30'N. e) 13°30'N.

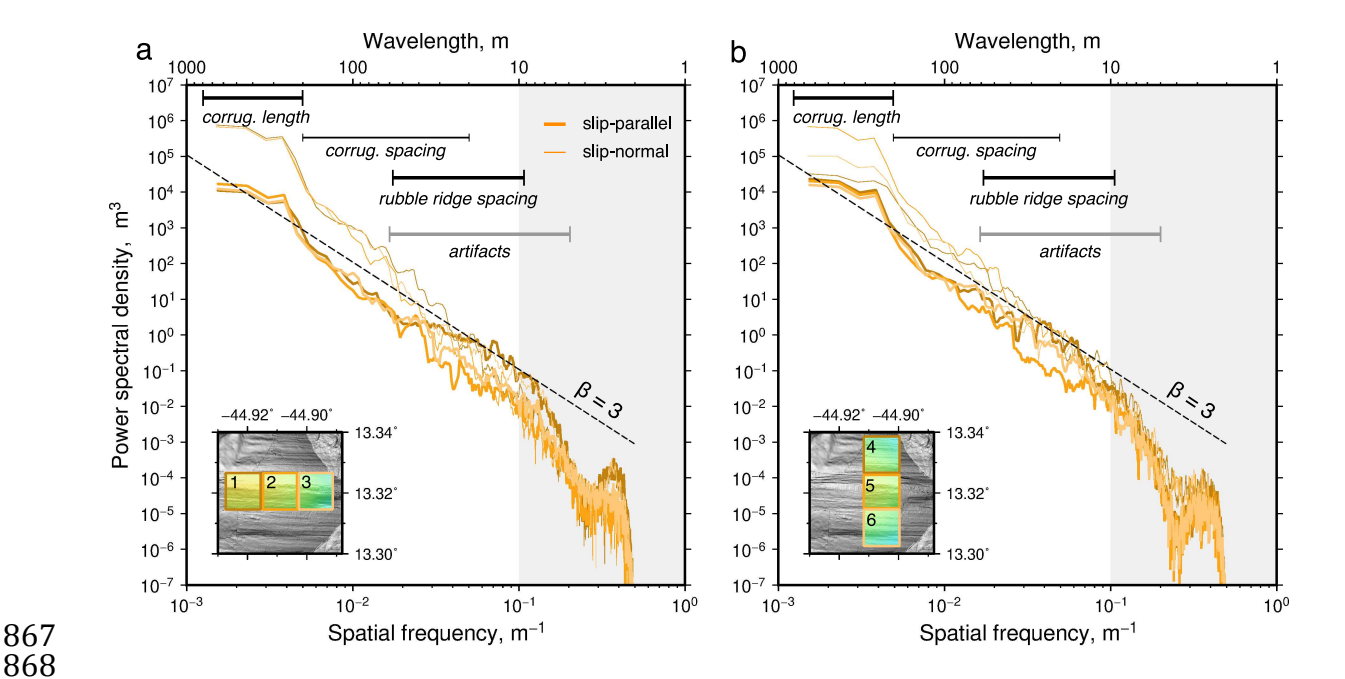
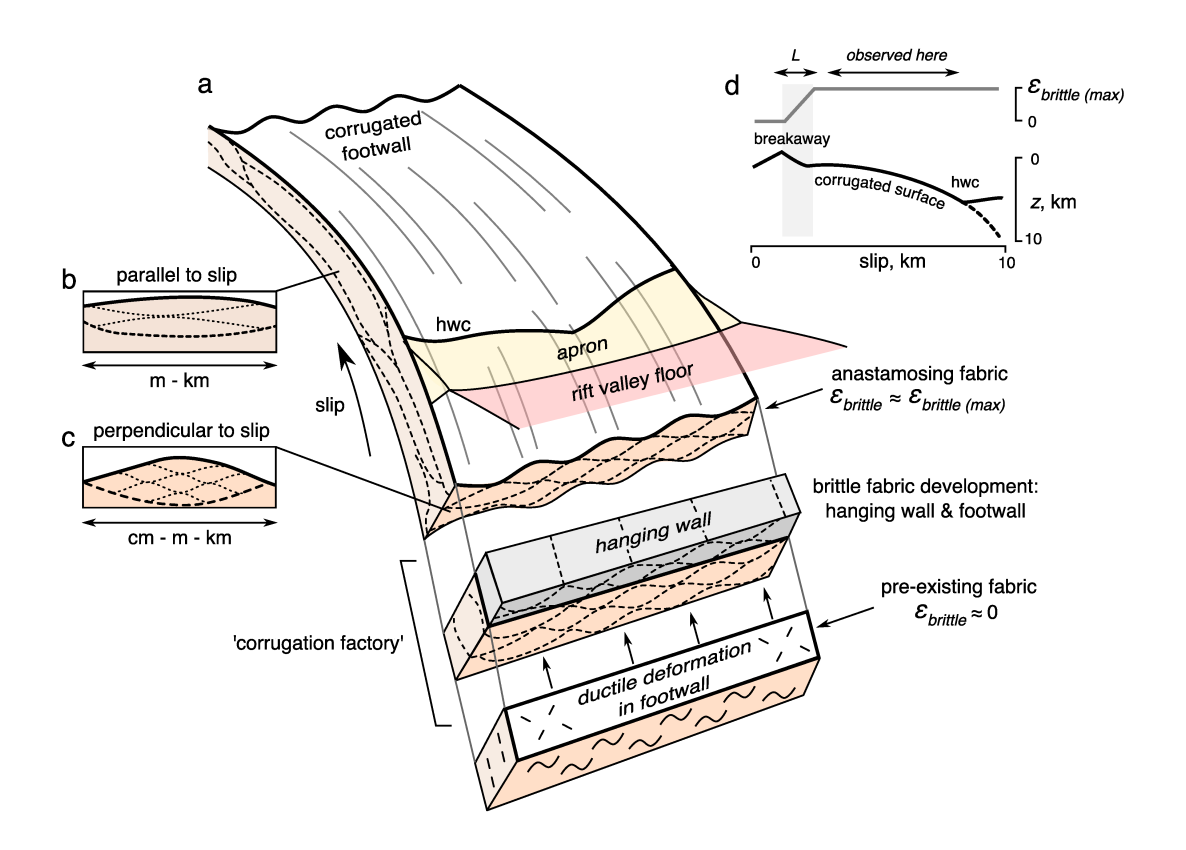


Figure 9. Power spectra along and across 13°20'N fault surface. a) Spectra from eastwest sequence of boxes (1.3 x 1.3 km in size; numbered 1, 2 and 3 in inset map); boxes are portions of fault surface that have experienced progressively more slip. Dark orange, orange and light orange boxes/spectra are boxes 1, 2 and 3, respectively; thick lines are slip-parallel, thin lines are slip-normal. Note increased power for slip-normal profiles at wavelengths of ~20–200 m, agreeing with observed corrugation spacing (thin bar); increased power wavelengths > 200 m on slip-parallel profiles, matching corrugation length (thick bar); increased power at wavelengths of 10–50 m for slip-parallel profiles in box 1 matching spacing of rubble ridges (thick bar). Gray bar indicates presence of possible multibeam artifacts at 5–50 m; gray band indicates region of noise where AUV navigation artifacts are prevalent, and data resolution insufficient to properly characterize individual features. b) Spectra from north-south sequence of boxes (numbered 3, 4 and 5 in inset map); Bars and abbreviations as in a).



895

896

897

898

899

900

901

902

903

904

905

906

907

908

909

910

Figure 10. Sketch illustrating corrugation genesis via strain localization. a) Perspective view through oceanic detachment fault, showing transition from footwall with preexisting ductile fabric (lower block), through corrugation factory (central block), and exhumation (upper curved block). White area is upper footwall surface, gray lines are corrugations; tan shading is footwall material, which acquires anastomosing fabric (dashed lines) after passing through corrugation factory; gray block is hanging wall material that also acquires anastomosing fabric; pink shading is rift valley floor (i.e., hanging wall); yellow shading is apron extending up to hanging-wall cutoff (hwc). b) and c) Insets showing anastomosing fabric oriented parallel and perpendicular to slip, respectively. d) Lower thick line is schematic bathymetric profile (based upon 13°20'N OCC), dashed line shows subsurface projection of fault surface. Upper solid line is brittle strain, ε , as a function of total slip; L is downdip extent of shear zone where strain is accumulated; gray shading highlights region of increasing strain, probably resulting in changing fault roughness beneath the breakaway/chaotic terrain (which are not observed here); arrow shows extent of data coverage from this study, where brittle strain is constant and relatively high, thus uniform fault roughness is expected.